

Violations of Weak Cosmic Censorship in Black Hole collisions

Tomas Andrade,^{1,*} Pau Figueras,^{2,†} and Ulrich Sperhake^{3,4,‡}

¹*Departament de Física Quàntica i Astrofísica, Institut de Ciències del Cosmos,
Universitat de Barcelona, Martí i Franquès 1, 08028 Barcelona, Spain*

²*School of Mathematical Sciences, Queen Mary University of London, Mile End Road, London E1 4NS, United Kingdom*

³*DAMTP, Centre for Mathematical Sciences, University of Cambridge, Wilberforce Road, Cambridge CB3 0WA, UK*

⁴*California Institute of Technology, Pasadena, California 91125, USA*

We study collisions of boosted rotating black holes in $D = 6$ and 7 spacetime dimensions with a non-zero impact parameter. We find that there exists an open set of initial conditions such that the intermediate state of the collision is a dumbbell-like horizon which is unstable to a Gregory-Laflamme-type instability. As is usually the case for similar unstable configurations, the evolution of such an instability leads to a pinch off of the horizon in finite asymptotic time, thus forming a naked singularity. Hence, this is the first fully genuine violation of Weak Cosmic Censorship conjecture in higher dimensional asymptotically flat spacetimes.

Introduction.—General Relativity (GR) governs the large scale structure of our Universe. Despite its enormous success, the fact that singularities can be generically formed in dynamical settings [1] in principle calls into question its predictive power. Motivated by this, Penrose postulated the “Weak Cosmic Censorship (WCC) Conjecture” [2], which proposes that singularities formed in dynamical evolution must be hidden inside black hole (BH) horizons. This constitutes a key link between the singularity theorems and the ubiquitousness of astrophysical black holes, for which Penrose was recently awarded the Nobel prize. Through active investigation in over half a century, counter-examples to WCC in settings beyond astrophysics have been found, which can be regarded as a possibility to access the quantum regime of gravity, at least theoretically. They fall into two major categories: i) critical collapse, which involves fine tuning of initial data such that a zero mass singularity is formed in $4D$ and above [3]; ii) death by fragmentation, which results from elongated horizons becoming unstable and eventually pinching off in finite time. The latter category will be the main focus of our letter.

The instability which drives the initial stages of this phenomenon was famously discovered by Gregory and Laflamme (GL) [4], who showed that, in $5D$ and above, thin enough black strings (and p -branes in general) have exponentially growing linear modes that trigger spatial modulation along the horizon, in a way that resembles the Rayleigh instability in fluids [5, 6]. Later on, [7] followed the unstable black string into the non-linear regime by means of a numerical simulation, which provided convincing evidence in favour of the pinching off of the horizon in finite time. Moreover, the authors observed the formation of BH satellites joined by thin necks organized in a fractal structure. It is by now understood that not only strings, but all elongated horizons which are locally string-like and thin enough, present these unstable modes, e.g., black rings [8], and ultra-spinning BHs [9–14]. The full non-linear evolution of such unstable configurations has been studied in [15–17], concluding in all these scenarios that the horizon pinches off in finite time, in a way similar to the black string case.

All of the above setups have in common that the starting point is an unstable configuration. Therefore, one may wonder if the so-obtained singularities are a truly natural feature of the evolution in GR. Along these lines, a new mechanism

for violation of WCC has been recently proposed [18, 19]: the collision of BHs in higher dimensions. What the authors noted is that, if the total angular momentum is high enough, an elongated horizon should form as an intermediate, long-lived, state after the collision. After this point, the horizon could undergo the breaking described above, depending on the competition between radiation of mass and angular momentum, and the GL instability. The former tends to make the horizon rounder and shorter, thus taming the effect of GL. Since radiation is exponentially suppressed with D , and the growth rates of the GL instability remain relatively constant, this mechanism is guaranteed to work if D is sufficiently large. On the other hand, this behaviour is absent in head-on collisions in four or higher dimensions [20, 21], and in grazing BH collisions in $4D$ [22], none of which exhibit elongated horizons or any signs of censorship violation even when colliding above 90 % of the speed of light. Uncovering exactly when and how the proposed phenomenon takes place, requires fully-fledged numerical GR techniques. We note that bar mode instabilities of rotating black holes are known in $6D$ and above [13, 14], so elongated horizons are more likely to exist in $D \geq 6$. For a sufficiently large initial angular momentum, these unstable ‘bar-shaped’ black holes develop a local GL instability. During the evolution of this instability, only about 5% of the total mass of the system is radiated, which is insufficient to prevent the formation of a naked singularity in finite time [17]. Furthermore, Ref. [21] reports that for $v \leq 0.6$ the radiation emitted in head-on collisions is below 1%. All of this considered, we envision that intermediate velocities, relatively high intrinsic spins and impact parameters, and $D \geq 6$ constitute a favourable region for WCC violation in parameter space.

Here we undertake the task of numerically simulating the collision of $6D$ and $7D$ stable, single-spinning BHs with a finite impact parameter. This initial setting is closely analogous to that of a BH binary merger in $4D$, but the dimensionality gives rise to striking differences in the evolution as we now describe. We identify, within a significant proportion of the parameter space, configurations that form an elongated horizon shortly after the merger, which breaks through the further evolution of a local GL instability. This process does not require any fine tuning. Moreover, we observe that the late time dynamics resemble the end point of the black strings and ultra-spinning BHs of [15–17]. In particular,

we observe the formation of two well-defined generations of satellites, and the beginning of a third one. Each generation consists of spherical blobs joined by thin tubes, which can be approximated by quasi-stationary BHs and strings, respectively. The last stage to which we have access consists of a central rotating black object, joined by a thin horizon to two non-spinning blobs that move away from each other, see Fig 1. The thin tubes in the middle are stretching due to the motion of the outer blobs, and develop their own satellites. We see that each segment is GL unstable, so it is clear that the process will continue until the pinch off.

We extract the gravitational waves produced in the collision, finding two peaks. The first one is simply due to the merger of the BHs. The second peak produces a stronger signal, and we attribute it to the sudden change of angular velocity and shape of the elongated horizon. Employing a toy model of a $D > 4$ dimensional binary which undergoes a qualitatively similar change in angular velocity and separation, we extract the radiated energy and observe a similar peak; cf. the Supplementary Material for more details. We find that the total radiated energy is strongly suppressed (it amounts to less than 1% in 7D), confirming the hypothesis that there is no mechanism to stop the formation of a naked singularity in finite asymptotic time.

Numerical methods.—We solve the vacuum Einstein equations in $D = 6, 7$ using the CCZ4 formulation as described in [23, 24]. We restrict ourselves to dynamics in 3+1 dimensions by imposing an $SO(D-3)$ symmetry by means of the modified cartoon method [13, 25, 26]. The conventions for the damping parameters κ_1 and κ_2 , and choice of gauge evolution are those of [17]. We construct the initial data by superimposing two boosted Myers-Perry (MP) BHs [27] written in Kerr-Schild (KS) coordinates, as described in [28]. This yields a mild violation of the constraints in the initial surface, but in higher dimensions it can be easily remedied as we describe below. We begin with a single, unboosted MP BH with mass and rotation parameters μ, a , whose relation to the mass and angular momentum are given in Eq. (9) in the Supplementary Material. We write the metric as

$$g_{\mu\nu} = \eta_{\mu\nu} + f(\mathbf{x})k_\mu k_\nu, \quad (1)$$

where η is the Minkowski metric, f is a function of the space-time coordinates \mathbf{x} and k^μ is a null vector. The explicit expressions for f and k^μ are given in Ref. [27]; see also the Supplementary Material for details. For this form of the metric, we can boost the BH by simply applying the corresponding Lorentz transformation to each of the vectors k^μ in Eq. (1). Henceforth, we split the coordinates as t, x, y, z, w_i where ∂_{w_i} are “cartoon” directions in the language of [26], and choose a single spin aligned with the z -axis.

Without loss of generality, we place one of the BHs at $(x_0, y_0, 0)$ and give it an initial velocity along the x -direction, which we denote by v . We ease the tracking of the dynamics by choosing symmetric data in which the second BH is positioned at $(-x_0, -y_0, 0)$ with speed $(-v, 0, 0)$, which gives an orbital angular momentum pointing in the z -direction. Both black holes have intrinsic spin along the z -direction, with spin parameter a . We emphasise that in our

setting the orbital and intrinsic angular momenta are aligned, which allows us to achieve higher values of the total angular momentum. The impact parameter is controlled by y_0 . Moreover, recall that in $D > 4$ there is no inspiral phase in binaries [29], which means that, generically, BHs interact only if y_0 is sufficiently small. While x_0 does not play a fundamental role, we need to choose it such that the initial BHs are sufficiently far apart so that the constraint violations on the initial surface as a result of simply superposing two MP BHs are small. In addition, having a sufficiently large x_0 allows us to decouple the initial gauge dynamics from the collision; our gauge conditions result in an adjustment phase lasting about $3\mu^{1/(D-3)}$.

Our main observable of interest is the location of the apparent horizon (AH). Tracking it from first principles entails solving a non-linear PDE in two variables at a given instant of time. Shortly after the collision of the two BHs, the common AH evolves into a non-star-shaped surface, with increasingly complex structure as shown in Fig. 1; there exist as yet no algorithms to find the AH for such surfaces. In this letter we therefore borrow from the results of [17] which have provided convincing evidence in a variety of scenarios that the location of the AH matches within a few percent with a contour of the conformal factor χ . While there is some dependence on the space-time dimension D , this has been observed to be mild [15–17]. Motivated by this, we will refer to the location of the “apparent horizon” by the location of the contour $\chi = 0.6$. We provide further details in the Supplementary Material.

We are also interested in the pattern of the gravitational waves produced by our collisions. For their extraction, we follow Ref. [17] and evaluate the appropriate integrals of the components of the Weyl tensor projected on a basis of spherical harmonics. We focus on the components $\Omega'_{(A)(B)}$ of the Weyl tensor along null rays projected onto a basis of spherical harmonics $Y_{\ell\dots}^{(A)(B)}$ according to

$$\Omega'_{\ell\dots} = \lim_{r \rightarrow \infty} r^{(D-2)/2} \int d\Omega_{(n)} Y_{\ell\dots}^{(A)(B)*} \Omega'_{(A)(B)}. \quad (2)$$

Here $\ell\dots$ denotes the set of quantum numbers of the spherical harmonics and $d\Omega_{(n)}$ is the volume element of the n -sphere. We record the relevant tensor harmonics for the 5-sphere in the Supplementary Material, while the $n = 4$ case can be found in [17].

We implement the numerical scheme in *GRChombo* [30, 31], using up to twelve levels of refinement with a 2:1 refinement ratio. We add the extra levels to better resolve the spatial gradients thus keeping the regions of constraint violations far away from the $\chi = 0.6$ surface, which we use as a proxy for the horizon. We ensure that the region contained within this contour is covered by at least 40 grid points. Unacceptably large constraint violations due to insufficient resolution lead to unphysical effects, such as a rapid swelling of the horizon. We have checked the robustness of our results by introducing refinement levels at different times, provided that the extra levels are added whilst the constraint violation region is sufficiently small. Following [15–17], we apply artificial diffusion in the region $\chi \leq 0.075$ to keep the constraint violations under control. We have employed cubic

computational domains, with side L . The x and y are standard Cartesian coordinates, upon which we impose Sommerfeld boundary conditions at the edges of the domain. At $z = 0$ we impose the regularity conditions as required by the Modified Cartoon Method, while at $z = L$ we impose Sommerfeld boundary conditions. We perform the time evolution using the fourth order Runge-Kutta method (RK4). The remaining parameters of our simulations are as in [17].

Results.—For both $D = 6, 7$ we have explored the space of parameters a, v, y_0 by running some low resolution simulations until we observe the formation of a long bar-like horizon after the merger. As mentioned above, no fine tuning is required in order to achieve such states. Out of the parameters explored, we have selected three study cases to continue the evolution further with the aid of higher resolution simulations. We shall discuss in the main text the $D = 7$ case, for which we have been able to follow the late stages of the evolution for longer times. We discuss the $D = 6$ cases in the Supplementary Material, for which we have obtained qualitatively similar results.

Henceforth we measure time and distance in dimensionless form using the mass parameter μ of a single member of our BH binary. Specifically, we display time in the form of $t = \tilde{t}/\mu^{1/(D-3)}$, where \tilde{t} is coordinate time in geometric units, and likewise for radius r and Cartesian coordinates x, y, z . Our $D = 7$ collision is characterized by initial data with parameters $v = 0.5, a = 0.7, y_0 = 1.1, x_0 = 10$. Note that the spin is within the stability bound $a_{\max} = 0.74$ reported in [14]. First, we have performed a simulation in a small domain of cubic size $L = 64$, including up to 10 levels. This simulation, displayed in Fig. 1, clearly shows that a dumbbell-shaped horizon forms after merger, consisting of two spherical blobs joined by a thin tube. Moreover, we observe the appearance of spatial modulation along the horizon, characteristic of the GL instability. At the same time, the length of the dumbbell increases making the middle tube thinner, which accelerates the effect of the instability. Continuing the evolution further, we have been able to see the formation of two generations of satellites, e.g., small spherical beads joined by thin tubes, closely resembling the late stages of unstable strings and ultra-spinning BHs. Our numerics have allowed us to observe the onset of a third generation, in which all string segments present in the second generation, develop their own local GL instability. Note that in $7D$, the critical value for the width over length ratio of strings which are GL unstable is $r_{GL,7D} \equiv \text{width}/\text{length} \approx 0.5$. We have explicitly checked that the string segments present in our first and second generation are well below this value.

In order to extract the gravitational waves, we have increased the size of the computational domain to $L = 256$, adding two levels in order to achieve equal resolutions at the horizons of the BHs. We have extracted the waves at radii $R = 25.0, 27.5, 30.0$ and observed the expected linear behaviour: all three wave forms match in all channels after the corresponding time shifts. We display the results for the $D = 7$ case in Fig. 2. Interestingly, we observe an initial regime in which small waves arrive for which this matching property does not hold. This corresponds to the initial constraint violations from superposing the two MP BHs and to

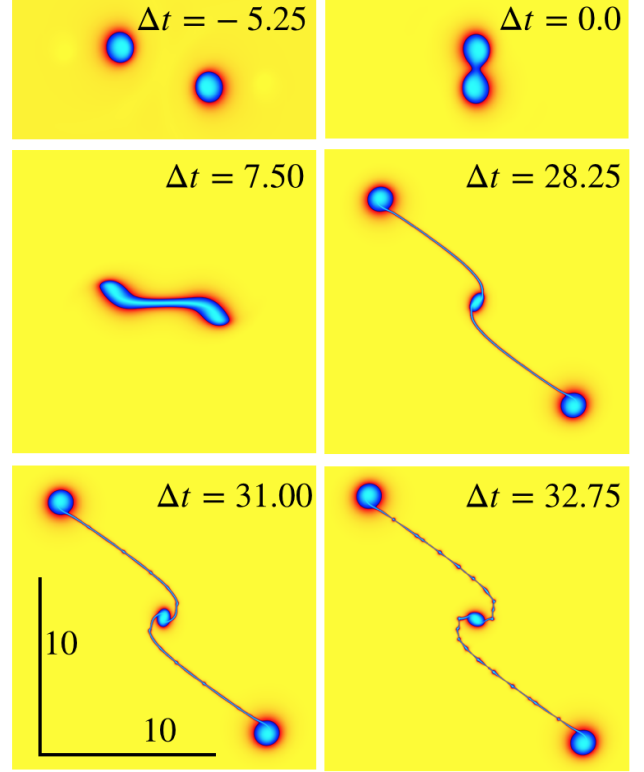


FIG. 1. Snapshots of the $7D$ evolution with $v = 0.5, a = 0.7, b = 2.2$, at times $\Delta t = t - t_{\text{merger}}$. They correspond to: initial condition, merger, bar formation, first generation, second generation, latest stage. We show a spatial length of 10 units on the bottom left panel.

the adjustment of the gauge, and it is unphysical.

In Fig. 2, we observe the first physical peak of radiation produced in the $m = 2$ channel for $\ell_5 = 2, 4$ at $t - t_{\text{merger}} \sim 30$, corresponding to the “collision” of the two BHs, when a common enveloping horizon first appears. As shown in the second panel in Fig 1 (see also the first panels in Figs. 5 and 6) this common horizon is dumbbell shaped. Furthermore, this resulting BH is rotating since it acquires part of the total angular momentum of the initial state, whilst some of the angular momentum has already been radiated away. At some point, which depends on the initial total angular momentum (and the number of dimensions D), the BH stops rotating and the neck connecting the two bulges starts expanding, producing a second radiation peak; in the $D = 7$ example of Fig. 2, this happens at around $t - t_{\text{merger}} = 7.5$. We confirm this picture with a simple model; see Supplementary Material.

Up until and including the second peak, the total radiated energy is about 0.01% of the Arnowitt-Deser-Misner (ADM) mass, see Fig 7, which follows from the data in Fig. 2 using eq. (24). We expect radiation emitted at later stages to amount to a smaller fraction, since the dynamics of the outer blobs is quasi-stationary, and the GL cascade taking place in the strings produces very little radiation ([17] reports that less than 5% of the total ADM mass is radiated during the last stage of GL in the $6D$ evolution of ultraspinning BHs). We discuss this issue further in the Supplementary Material, where we provide a crude upper bound. In summary, the effects of radiation are sufficiently suppressed in $D \geq 6$, so

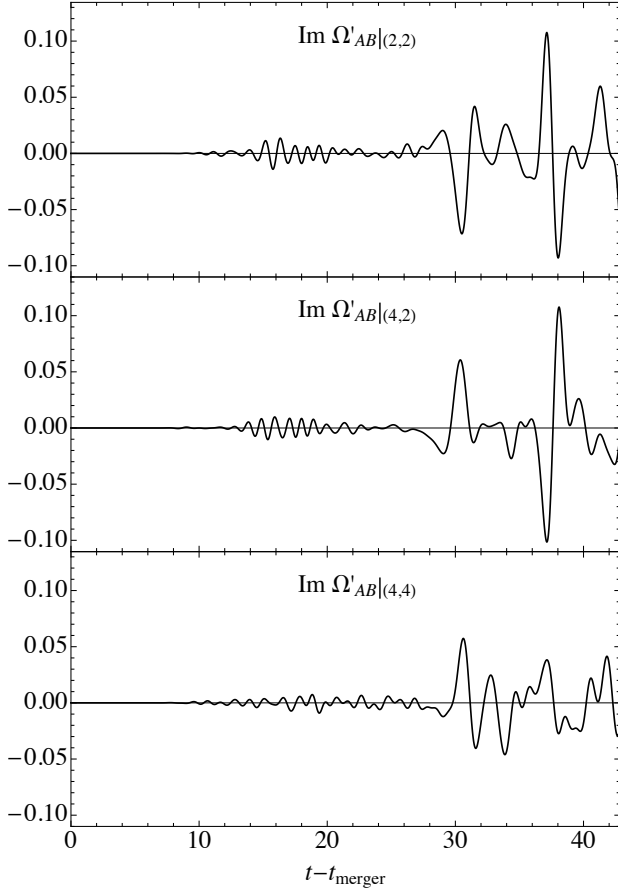


FIG. 2. Imaginary part of the projection of the matrix of Weyl scalars Ω'_{AB} onto the harmonics $(\ell_5, m) = (2, 2), (4, 2), (4, 4)$ for the collision in $D = 7$ (see Supplementary Material). In these plots, the extraction was done at a radius $R = 30$ from the center of the grid. The first peak is observed at $t - t_{\text{merger}} \sim 30$, corresponding to the initial collision of the two BHs; the oscillations observed before this time are due to the constraint violations in the initial data and initial gauge adjustment. Two large peaks are observed at around $t - t_{\text{merger}} \sim 37.5$, which corresponds to time at which the dumbbell-shaped horizon stops rotating and starts expanding. Beyond this point, whilst the gravitational wave signal continues to develop new features corresponding to the onset and further evolution of the GL instability in the neck, their amplitude is never as large as that of these two initial peaks. Consequently, the energy loss in absolute value decreases.

that there is no mechanism to stop the violation of WCC in BH collisions provided the initial angular momentum is sufficiently large.

Discussion.—By means of numerical GR simulations, we have been able to establish the violation of the WCC conjecture in BH collisions for $D = 6, 7$. The driving mechanism is the GL instability, and the dynamics unfold in close parallel to other known cases of horizon pinching off. We have observed the formation of two generations of satellites and the beginning of a third one, which further improves our understanding of the dynamical process. We have extracted the gravitational waves emitted by the binaries, showing that there is a second peak which surpasses the burst due to the merger. After this second peak, we expect the emission of radiation to be small, paving the way for the GL instability

to break the horizon. Since radiation is further suppressed in higher dimensions, our results strongly indicate that the violation of WCC we have identified is present in all $D \geq 6$. However small, the emission of gravitational waves in our setting has revealed interesting features, and we expect to study this issue further – in particular, the radiation produced during the formation of satellites – in future work.

It is remarkable that the large D effective theory [32–34], out of which the arguments for this mechanism were originally drawn [18, 19], is able to capture the qualitative dynamics so well. In our context, the main drawback of the effective theory is the non-perturbative character of radiation. In hindsight, perhaps the main reason for its success in predicting the violation of WCC is the relatively small role that radiation plays already in $6D$.

As in all other known cases of WCC violation by fragmentation of horizons, the regions which we expect to become Planckian are “small” at least with respect to the size defined by the geometry of the apparent horizon. In the language of [35], they correspond to mild violations of WCC, which means that any suitable quantum resolution (analogue of the evaporation of a droplet in hydrodynamics) will have a small effect on the subsequent (classical) dynamics. In this sense, although the more strict version of the WCC conjecture is violated (naked singularities do appear in the course of evolution), its spirit is salvaged (the lack of predictability that the violations entail is very small).

The case of $D = 5$ is special in various ways. Classically, the decays of the angular momentum barrier and the gravitational potential for point particles exactly match ($\sim r^{-3}$). Consistent with this general observation, no “zoom-whirl” orbits (i.e. long inspirals which result in mergers or scattering to infinity) have been found [36]. Moreover, no linear instabilities of 5D of single spinning MP BHs have been identified [14, 17], which in turn suggests that in this dimension black bars do not exist, as opposed to $D \geq 6$ [13]. These facts, and the observation that radiation is less suppressed with respect to $6D$, suggest that the violations of WCC reported here, should at least behave quite differently in $5D$, if present at all.

An interesting technical point which we have not addressed here is the derivation of the location of the apparent horizon from first principles. As discussed above, this requires parametrizing the shape of a reference surface, which is challenging in scenarios like ours where spatial modulation is constantly changing the shape of the horizon. Obtaining the apparent horizon in this way would allow us to accurately study entropy production. We leave these interesting issues for future research.

Acknowledgments.—We thank Roberto Emparan for many insightful discussions. Our special thanks are for the entire GRChombo collaboration (www.grchombo.org) for their help and support. TA is supported by the ERC Advanced Grant GravBHs-692951. He also thanks QMUL for the hospitality during the early stages of this project. PF is supported by the European Research Council Grant No. ERC-2014-StG 639022-NewNGR, by a Royal Society University Research Fellowship (Grant No. UF140319 and URF\R\201026) and by a Royal Society Enhancement

Award (Grant No. RGF\EA\180260). US acknowledges support from the European Union's H2020 ERC Consolidator Grant "Matter and strong-field gravity: new frontiers in Einstein's theory" Grant No. MaGRaTh-646597, the STFC Consolidator Grant No. ST/P000673/1, and the GWverse COST Action Grant No. CA16104, "Black holes, gravitational waves and fundamental physics". The simulations presented here were done on the MareNostrum4 cluster at the Barcelona Supercomputing Centre (Grant No. FI-2020-2-0011 and FI-2020-2-0016), the SDSC Comet and TACC Stampede2 clusters through NSF-XSEDE Grant No. PHY-090003, and the Cambridge Service for Data Driven Discovery (CSD3), part of which is operated by the University of Cambridge Research Computing on behalf of the STFC DiRAC HPC Facility (www.dirac.ac.uk). The DiRAC component of CSD3 was funded by BEIS capital funding via STFC capital grants ST/P002307/1 and ST/R002452/1 and STFC operations grant ST/R00689X/1. DiRAC is part of the National e-Infrastructure.

SUPPLEMENTARY MATERIAL

Initial data.—For D even, the metric in Kerr-Schild form for a single BH is given by Eq. (1) with

$$f = \frac{\mu r}{\Pi(r)F(r, x^i)}, \quad (3)$$

$$\Pi(r) = \Pi_i^{(D)}(r^2 + a_i^2), \quad (4)$$

$$F = 1 - \sum_{i=1}^{s(D)} \frac{a_i^2(X_i^2 + Y_i^2)}{(r^2 + a_i^2)}, \quad (5)$$

$$k = dt + \sum_{i=1}^{s(D)} \frac{\{r(X_i dX_i + Y_i dY_i) + a_i(X_i dY_i - Y_i dX_i)\}}{r^2 + a_i^2} + \frac{zdz}{r}, \quad (6)$$

where $k = k_\mu dx^\mu$, $s(D) = (D-2)/2$, and X_i, Y_i denote subsets of the coordinates that specify the rotation planes; they will be specified explicitly below. The index i runs from $1..(D-2)/2$, and corresponds to the number of possible rotation planes, in such a way that a non-vanishing a_i adds rotation on the axis orthogonal to (X_i, Y_i) . We explicitly display the sum over i to emphasise that there is no extra summation of repeated indices. The quantity denoted by r is not an independent coordinate, but can be expressed in terms of the X_i, Y_i by means of the condition $k_\mu k_\nu \eta^{\mu\nu} = 0$. In order to implement the modified cartoon method in $D=6$, we choose $a_i = (a, 0)$, $X_i = (x, w_1)$, $Y_i = (y, w_2)$ with w_1, w_2 being isometric directions. This gives the BH rotation along the z -axis. Finally, we use a translation $(x', y') = (x - x_0, y - y_0)$ and a Lorentz boost along x ,

$$t'' = tc_\eta + x's_\eta, \quad x'' = -ts_\eta + x'c_\eta \quad (7)$$

with $c_\eta = \cosh \eta$, $s_\eta = \sinh \eta$ and $\cosh \eta = (1 - v^2)^{-1/2}$.

For odd D , we have Eqs. (3)–(5) along with

$$k = dt + \sum_{i=1}^{s(D)} \frac{\{r(X_i dX_i + Y_i dY_i) + a_i(X_i dY_i - Y_i dX_i)\}}{r^2 + a_i^2} \quad (8)$$

and now the number of rotation planes is $s(D) = (D-1)/2$. To implement the cartoon method in $D=7$, we choose $a_i = (a, 0, 0)$, and $X_i = (x, z, w_1)$, $Y_i = (y, w_2, w_3)$, where (w_1, w_2, w_3) parametrize the isometric directions. This gives the BH rotation along the z -axis.

The mass and angular momentum for a single spinning BH are given by

$$M = \frac{(D-2)\Omega_{D-2}}{16\pi G}\mu, \quad J = \frac{2}{(D-2)}Ma, \quad (9)$$

where

$$\Omega_{D-2} = \frac{2\pi^{(D-1)/2}}{\Gamma[(D-1)/2]}. \quad (10)$$

Apparent horizons and contours of χ .— In this section we provide some more quantitative details of the relation between the apparent horizon (AH) and the contours of the conformal factor χ . This relation is gauge dependant. We have observed that it works in traditional $1 + \log$ slicing plus Gamma driver gauges used in numerical relativity in a variety of contexts, ranging from astrophysical BH binaries in 3+1 dimensions to studies of BH instabilities in higher dimensions [15–17].

As pointed out in the main text, the fact that the AH, that forms in the collisions that we study in this Letter (see Figs. 1, 6, 5), is a non-star-shaped, highly complex and rapidly changing surface makes the problem of finding it particularly challenging. One possible way forward is to consider a reference surface with the approximate shape of the AH [37, 38]. However, in our case, the reference surface should capture some of the key features that appear as a consequence of the GL cascade; since the latter develop randomly on different scales, both in time and space, finding a suitable reference surface at each time step seems impractical. Alternatively, one could use an intrinsic parametrization of the surface and impose some gauge condition (e.g., harmonic) to fix the reparametrization freedom as in [16]. However, in this reference it was found that the resulting system of equations was not very robust in practice in spite of being manifestly elliptic. Therefore, the problem of parametrizing and finding the AHs that generically appear in higher dimensional BH physics remains open. As we will explain below, a promising avenue would be to use certain contours of the evolved variable χ as the reference surface. This approach would have the advantage that these contours capture some of the key features of the AH at any given instant of time and they are readily available since χ is one of the evolved variables. Implementing this in practice is beyond the scope of this Letter and we leave it for future work. In the following, we will provide quantitative evidence that the $\chi = 0.6$ contour does indeed capture the essential features of the AH's shape. Other contours, such as $\chi = 0.5$ or $\chi = 0.4$, would also be comparatively informative. This insensitivity to the specific value of the contour is due to the steep gradients of the metric fields in higher-dimensions.

In Fig. 3 (top) we show the values of χ on the AH near the endpoint of the ultraspinning instability of a MP BH in 6D with an initial spin parameter $a/\mu^{1/3} = 1.85$ reported by one

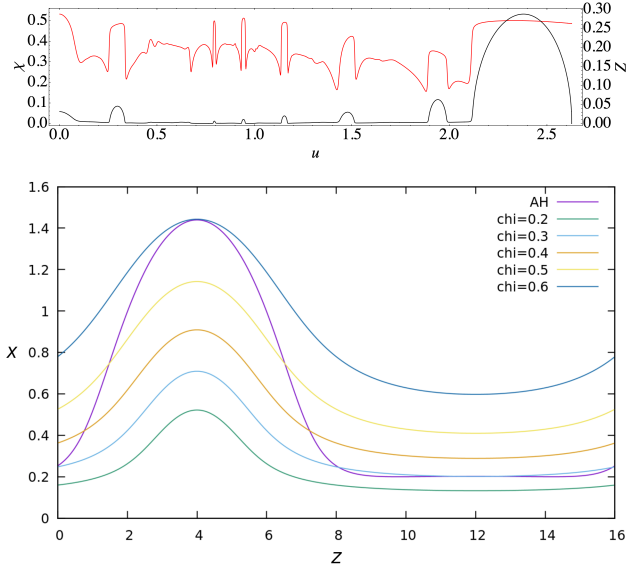


FIG. 3. *Top*: χ (in red) on the AH plotted against the embedding coordinate u near the endpoint of the ultraspinning instability of a MP BH in 6D with an initial spin parameter $a/\mu^{1/3} = 1.85$ (see [16] for more details); the Z coordinate of the embedding is shown in black and it serves to guide the eye. This figure shows that on the AH, $\chi \sim 0.5$ on the blobs and $\chi \sim 0.3$ on the necks. *Bottom*: AH and several χ contours during the evolution of the GL instability of a black string in 5D.

of us in [16]. The shape of the AH is shown in black. This plot shows that the $\chi = 0.5$ contours capture the ‘bulges’ quite accurately, especially those from the early generations that have reached a quasi-stationary state. On the other hand, the $\chi = 0.3$ contours capture the neck regions of the AH. In the bottom plot of Fig. 3 we depict the AH together with different χ contours at some instant of time during the evolution of the GL instability of a black string in 5D [39]. This plot shows that indeed these contours of χ capture that key features of the AH in the evolution of the GL instability, in this case of a black string. We want to highlight that in the *top* and *bottom* panels in Fig. 3 we consider completely different systems, namely a rotating spherical asymptotically flat BH in 6D and a black string in 5D; the fact that in both cases the same contours of χ capture the shape of the AH makes us confident that results in this Letter based using the $\chi = 0.6$ contour as a proxy for the actual AH are robust.

Finally, in Fig. 4 we compare the $\chi = 0.6$ (in blue), $\chi = 0.5$ (in black) and the $\chi = 0.3$ (in red) contours for the 7D BH collision described in the main text. According to the previous discussion, the $\chi = 0.6$ contour should accurately capture the shape of AH in the bulges, especially those of the early generations which have already reached a quasi-stationary state. We used this contour of χ to estimate the masses and angular momenta of the big bulges. On the other hand, the $\chi = 0.3$ contour should capture the shape of the AH on the neck regions. In fact, both contours are very close to each other in the neck regions and both capture the most salient features of the shape of the AH.

6D case.—In this section we discuss the results we have

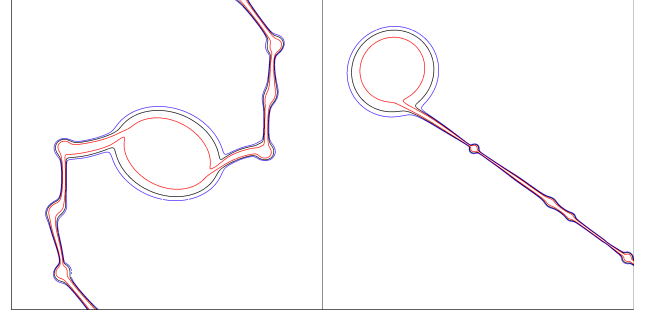


FIG. 4. Comparison of the $\chi = 0.6$ (in blue), $\chi = 0.5$ (in black) and $\chi = 0.3$ (in red) contours for the the 7D BH collision reported in the main text. The $\chi = 0.6$ contour should track the AH near the bulges whilst the $\chi = 0.3$ should do so in the necks. The key features of the AH are captured by both contours; in particular, in the neck regions the two contours are very close to each other.

obtained in $D = 6$. As mentioned in the main text, our results are qualitatively similar to the $D = 7$ case, in that we also see strong evidence for the pinching off of the horizon in finite asymptotic time. We have run two detailed simulations in cubic domains of size $L = 64$, with collision parameters $\{v = 0.5, a = 0.6, b = 2.5\}$, $\{v = 0.45, a = 0.7, b = 2.5\}$, respectively. Note that both of these values of a are well within the stability regime for rotating MP BHs $a_{\max} = 0.73$ [14]. In Figs. 5, 6 we show representative snapshots of χ on the $z = 0$ plane. In the simulation shown in Fig. 5, the formation of the first generation of satellites is clear, and we observe that the dynamics closely resemble the 7D case. The critical dimensionless ratio for GL instability in this dimension is $r_{GL,6D} \equiv \text{width}/\text{length} \approx 0.4$. Estimating this value for $t = 13.6$ in Fig. 5, $r_{GL} \approx 0.02$, showing that this string is well in the unstable regime. In the dynamics that follow, we again observe the appearance of the central rotating blob, joined to the outer blobs by thin strings. Our computational resources did not allow us to reach the same stage for the simulation in Fig. 6. However, we do observe a rapid thinning of the neck which should lead to the development of the GL instability as in the previous cases. In particular, for $t = 15.0$ in 6 we estimate for $r_{GL} \approx 0.04$, so the strings are unstable.

As emphasised in the main text, there was no fine tuning required to find configurations such as these in which the neck thins and the GL instability kicks in. Hence, we can comfortably claim that the effect that we report is generic.

Gravitational waves in 7D.—It is convenient to write the metric on the S^3 at infinity such that it has a manifest $SO(4)$ symmetry and one of its $U(1)$ ’s is aligned with the $U(1)$ on the rotation plane of the incoming MP BHs:

$$ds^2 = d\chi^2 + \sin^2 \chi d\phi^2 + \cos^2 \chi d\Omega_{(3)}^2, \quad (11)$$

where $d\Omega_{(3)}^2$ is the metric on the unit S^3 . As shown in [17], due to the symmetries of the spacetime, the gravitational wave signal is contained in the scalar derived tensor harmonics. Given the form of the metric (11), a convenient basis for

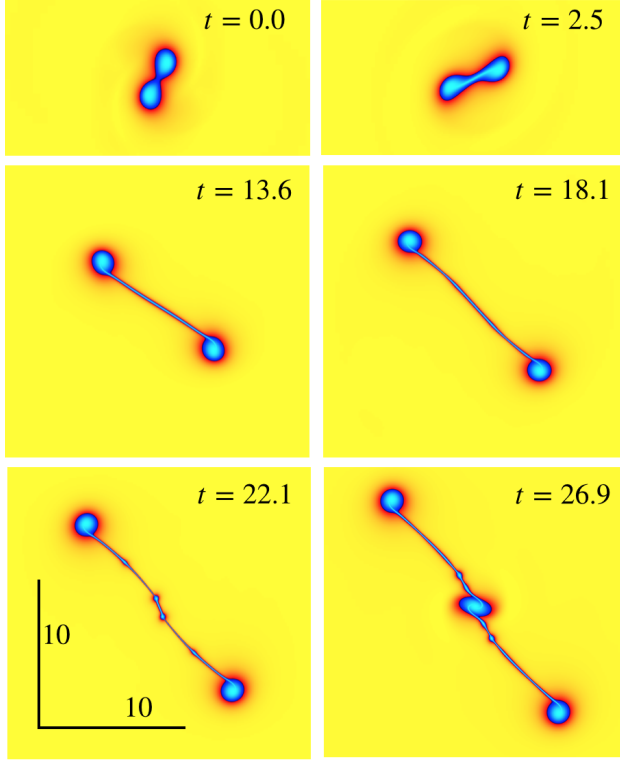


FIG. 5. 6D-A evolution with $v = 0.5$, $a = 0.6$, $b = 2.5$.

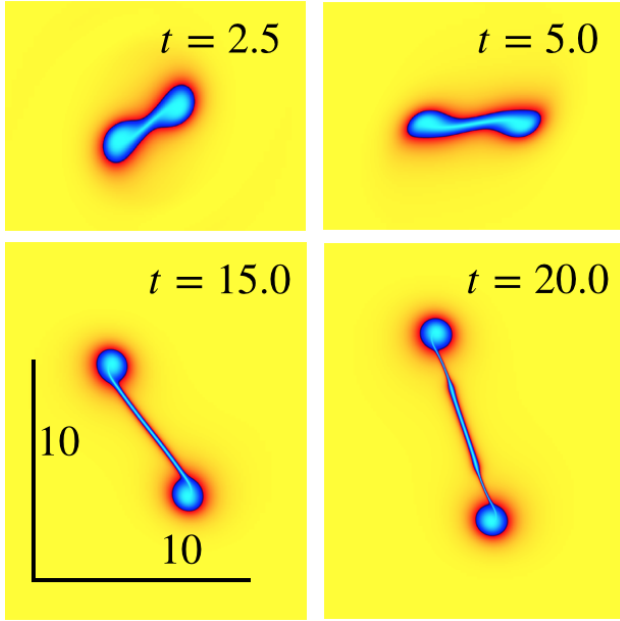


FIG. 6. 6D-B evolution with $v = 0.45$, $a = 0.7$, $b = 2.5$.

the scalar harmonics on the S^5 is

$$\mathbb{Y}^{\ell_5, m, \ell_3, \dots} = N e^{im\phi} (\sin \chi)^{|m|} (\cos \chi)^{\ell_3} \mathbb{Y}^{\ell_3, \dots} \times {}_2F_1\left(\ell_3 + |m| - k, k + \frac{3}{2}, \ell_3 + \frac{5}{2}; \cos^2 \chi\right), \quad (12)$$

where ${}_2F_1$ is a hypergeometric function, N is a normalization factor, k is a non-negative integer and $\mathbb{Y}^{\ell_3, \dots}$ are the scalar harmonics on the S^3 , so that $\Delta_{S^3} \mathbb{Y}^{\ell_3, \dots} = -\ell_3(\ell_3 + 2) \mathbb{Y}^{\ell_3, \dots}$; the dots in $\mathbb{Y}^{\ell_3, \dots}$ denote the remaining labels for quantum num-

bers of the harmonics. Regularity of the harmonics implies

$$\ell_5 = 2k - (\ell_3 + |m|). \quad (13)$$

Since the spacetimes that we consider in this paper preserve a round S^3 inside the S^5 , to extract the gravitational waves we only need to consider harmonics on the S^5 that also preserve a round S^3 . Therefore, from now on, in (12) we will consider harmonics with $\ell_3 = 0$ and hence we can uniquely label them with only two quantum numbers, (ℓ_5, m) .

Scalar derived traceless tensor harmonics on the n -sphere can be constructed from the scalar harmonics by [40]

$$\mathbb{S}_{ab}^{\ell_n, \dots, \ell_1} = \frac{\sqrt{n}}{\sqrt{(n-1)(\ell_n-1)(\ell_n+n)}} \times \left(\nabla_a \mathbb{S}_b^{\ell_n, \dots, \ell_1} + \frac{\sqrt{\ell_n(\ell_n+n-1)}}{n} g_{ab} \mathbb{S}^{\ell_n, \dots, \ell_1} \right), \quad (14)$$

where $\mathbb{S}_a^{\ell_n, \dots, \ell_1} \equiv \frac{1}{\sqrt{\ell_n(\ell_n+n-1)}} \nabla_a \mathbb{S}^{\ell_n, \dots, \ell_1}$ are the scalar derived vector harmonics, and g_{ab} is the metric on the unit S^n . The coefficients are chosen so that the scalar derived tensor harmonics are suitably normalized:

$$\int_{S^n} g^{ac} g^{bd} \mathbb{S}_{ab}^{\ell_n, \dots, \ell_1} \mathbb{S}_{cd}^{\ell'_n, \dots, \ell'_1} = \delta_{\ell_n \ell'_n \dots \ell_1 \ell'_1}. \quad (15)$$

To do the extraction, we need to compute the tensor harmonics on the S^5 in a certain basis of angular vectors. For the metric in (11), we choose the obvious basis,

$$m_{(1)} = \frac{\partial}{\partial \chi}, \quad m_{(2)} = \frac{1}{\sin \chi} \frac{\partial}{\partial \phi}, \quad m_{(i)} = \frac{1}{\cos \chi} \hat{m}_{(i)}, \quad (16)$$

where $\hat{m}_{(i)}$, $i = 1, 2, 3$ are a basis of angular (unit) vectors on the S^3 .

After these preliminaries, we are now ready to list the non-vanishing components of the scalar derived tensor harmonics on the S^5 that we have used to extract the gravitational waves:

- $(\ell_5, m) = (2, 0)$:

$$\begin{aligned} \mathbb{S}_{11}^{(2,0)} &= \frac{1}{\pi^{3/2}} \sqrt{\frac{3}{70}} [2 \cos(2\chi) + 1], \\ \mathbb{S}_{22}^{(2,0)} &= -\frac{1}{\pi^{3/2}} \sqrt{\frac{3}{70}} [\cos^2(\chi) - 4], \\ \mathbb{S}_{ij}^{(2,0)} &= -\frac{\delta_{ij}}{2\pi^{3/2}} \sqrt{\frac{3}{70}} [\cos(2\chi) + 3]. \end{aligned} \quad (17)$$

- $(\ell_5, m) = (2, 2)$:

$$\begin{aligned} \mathbb{S}_{11}^{(2,2)} &= \frac{1}{\sqrt{70}\pi^{3/2}} e^{2i\phi} [2 \cos(2\chi) + 3], \\ \mathbb{S}_{12}^{(2,2)} &= \frac{i}{\pi^{3/2}} \sqrt{\frac{5}{14}} e^{2i\phi} \cos(\chi), \\ \mathbb{S}_{22}^{(2,2)} &= -\frac{1}{2\sqrt{70}\pi^{3/2}} e^{2i\phi} [\cos(2\chi) + 9], \\ \mathbb{S}_{ij}^{(2,2)} &= \frac{\delta_{ij}}{\sqrt{70}\pi^{3/2}} e^{2i\phi} \sin^2(\chi). \end{aligned} \quad (18)$$

- $(\ell_5, m) = (4, 0)$:

$$\begin{aligned}\mathbb{S}_{11}^{(4,0)} &= -\frac{1}{2\sqrt{10}\pi^{3/2}} [\cos(2\chi) + 5\cos(4\chi) - 2], \\ \mathbb{S}_{22}^{(4,0)} &= \frac{1}{8\sqrt{10}\pi^{3/2}} [-24\cos(2\chi) + 5\cos(4\chi) + 3], \\ \mathbb{S}_{ij}^{(4,0)} &= \frac{\delta_{ij}}{24\sqrt{10}\pi^{3/2}} [28\cos(2\chi) + 15\cos(4\chi) - 11].\end{aligned}\quad (19)$$

- $(\ell_5, m) = (4, 2)$:

$$\begin{aligned}\mathbb{S}_{11}^{(4,2)} &= -\frac{1}{4\sqrt{5}\pi^{3/2}} e^{2i\phi} [2\cos(2\chi) + 5\cos(4\chi) - 2], \\ \mathbb{S}_{12}^{(4,2)} &= \frac{i\sqrt{5}}{16\pi^{3/2}} e^{2i\phi} [\cos(\chi) - 5\cos(3\chi)], \\ \mathbb{S}_{22}^{(4,2)} &= \frac{1}{16\sqrt{5}\pi^{3/2}} e^{2i\phi} [2\cos(2\chi) + 5\cos(4\chi) + 13], \\ \mathbb{S}_{ij}^{(4,2)} &= -\frac{\delta_{ij}}{4\sqrt{5}\pi^{3/2}} e^{2i\phi} \sin^2(\chi) [5\cos(2\chi) + 6]\end{aligned}\quad (20)$$

- $(\ell_5, m) = (4, 4)$:

$$\begin{aligned}\mathbb{S}_{11}^{(4,4)} &= \frac{1}{2\sqrt{2}\pi^{3/2}} e^{4i\phi} \sin^2(\chi) [2\cos(2\chi) + 3], \\ \mathbb{S}_{12}^{(4,4)} &= \frac{5i}{2\sqrt{2}\pi^{3/2}} e^{4i\phi} \sin^2(\chi) \cos(\chi), \\ \mathbb{S}_{22}^{(4,4)} &= -\frac{1}{4\sqrt{2}\pi^{3/2}} e^{4i\phi} \sin^2(\chi) [\cos(2\chi) + 9], \\ \mathbb{S}_{ij}^{(4,4)} &= \frac{1}{2\sqrt{2}\pi^{3/2}} e^{4i\phi} \sin^4(\chi).\end{aligned}\quad (21)$$

The harmonics with negative m can be obtained from the ones listed above by complex conjugation.

Finally, to do the extraction we compute the components of the matrix of Weyl scalars Ω'_{AB} in a certain orthonormal basis. We construct the latter starting from

$$\begin{aligned}m_{(1)} &= x\partial_x + y\partial_y + z\partial_z, \\ m_{(2)} &= xz\partial_x + yz\partial_y - (x^2 + y^2)\partial_z, \\ m_{(3)} &= -y\partial_x + x\partial_y,\end{aligned}\quad (22)$$

and carrying out a standard Gram-Schmidt orthonormalization [41]. The unit vectors on the transverse sphere direction are simply given by

$$m_{(\hat{i})} = \frac{1}{\sqrt{\gamma_{ww}}} \partial_{w_i}. \quad (23)$$

One can show that, asymptotically, the angular basis vectors obtained from (22) are aligned with (16).

Radiation peak due to separation.—In order to elucidate the origin of the second peak we observe in the pattern on gravitational radiation, we consider a simple model for a higher dimensional binary and use the quadrupole formula of [42]. Since a general expression is only available for even dimensions, we consider the case $D = 6$ which we expect will best capture the qualitative features of our setting.

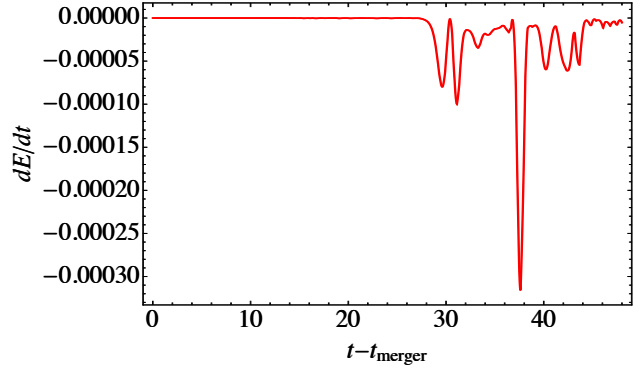


FIG. 7. Energy loss for our 7D simulation as computed at a radius $R = 30$ from the merger point. The large peak at $t - t_{\text{merger}} \sim 37.5$ is produced when the dumbbell-shaped BH stops rotating and starts expanding.

The quantity that we can readily compare is the energy loss dE/dt , which is related to the Weyl scalars as [43]

$$\frac{dE}{dt} = -\lim_{r \rightarrow \infty} \frac{r^{d-2}}{8\pi} \int_{S^{d-2}} \left(\int_{-\infty}^u \Omega'_{AB}(\hat{u}, r, x) d\hat{u} \right)^2 d\omega. \quad (24)$$

We show our results for the energy loss in $D = 7$ as computed from the Weyl scalars extracted from our numerics in Fig 7. The corresponding quadrupole formula for even D can be written as [42]

$$\frac{dE}{dt} = P(D) \left[(D-1) \partial_t^{\frac{D+2}{2}} M_{ij}(t) \partial_t^{\frac{D+2}{2}} M_{ij}(t) - \left| \partial_t^{\frac{D+2}{2}} M_{ii}(t) \right|^2 \right]. \quad (25)$$

where the prefactor is given by

$$P(D) = \frac{2^{2-D} (D-3) D}{\pi^{\frac{D-5}{2}} \Gamma\left[\frac{D-1}{2}\right] (D^2 - 1) (D-2)} G, \quad (26)$$

and

$$M^{ij} = \int d^{D-1} x T^{00}(t, x) x^i x^j. \quad (27)$$

In addition, [19] provided an expression for the emission of angular momentum in even dimensions, which in our case reduces to

$$\frac{dJ^{ij}}{dt} = \frac{4(D^2 - 1)}{D + 2} P(D) \left[\partial_t^{\frac{D+2}{2}} Q^{[i}_k \partial_t^{\frac{D}{2}} Q^{j]}_k \right], \quad (28)$$

where

$$Q^{ij} = M^{ij} - \frac{1}{D-1} \delta_{ij} M_{kk}. \quad (29)$$

In order to evaluate these expressions, we make the assumption that the energy distribution T^{00} is simply a delta function with support on two point particles that follow a trajectory on a two-dimensional plane. We parametrize the trajectory in polar coordinates $x_1(t) = \rho(t) \cos \theta(t)$, $x_2(t) = \rho(t) \sin \theta(t)$. For concreteness, we consider a circular binary which slows

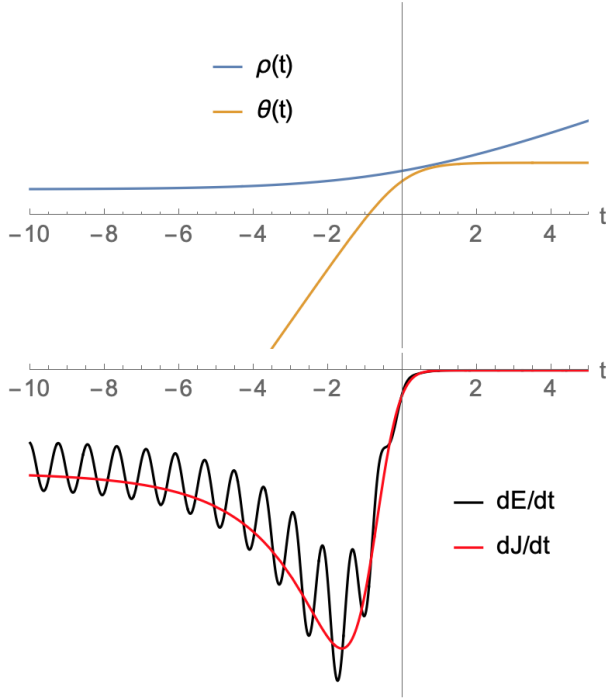


FIG. 8. *Top*: Trajectory for a binary which starts in a circular orbit and experiences a slow down and separation. (*Bottom*): Energy and angular momentum loss as computed from the quadrupole formulae (25), (28) in 6D.

down and separates along a straight line. This captures some of the qualitative features we observe in our simulations after merger. We show the profiles we have chosen for ρ and θ on Fig 8 (top) while the obtained pattern for energy and angular momentum loss is depicted on Fig 8 (bottom). At early times we observe a sinusoidal pattern for energy radiation characteristic of a circular binary. Interestingly, the later slow down and separation leads to a relatively sharp peak, which resembles the second radiation peak we observe in Fig 7. We also observe that the radiated angular momentum follows the pattern of the radiated energy averaged over the orbits.

Radiated energy and angular momentum.—We approximate the total initial and final mass and angular momentum according to

$$M_i = 2\gamma_i m_i, \quad (30)$$

$$M_f = 2\gamma_f m_f + m_{\text{central}} + 2m_{\text{string}}, \quad (31)$$

$$J_i = \gamma_i m_i \left[b_i v_i + 2 \frac{2}{D-2} a_i \right], \quad (32)$$

$$J_f = \left[\gamma_f m_f b_f v_f + \frac{2}{D-2} m_{\text{central}} a_{\text{central}} \right]. \quad (33)$$

Here m_i is the mass of the BHs in the initial state, with velocities v_i , spins a_i and impact parameter b_i —defined as the distance between the center of the BHs and the plane along which the binary is reflection symmetric, i.e. $b_i = y_0$ in the notation of the main text—, m_f is the mass of the BHs at the extremes of the final dumbbell, which have velocities v_f and impact parameter b_f (we have checked that they do not

have intrinsic spin), m_{central} , a_{central} are the mass and spin of the central BH, and m_{string} is the mass of each of the strings joining the central and outer BHs.

We assume the BHs and strings involved in this calculation to be stationary, in which case we can compute their properties from Eq. (9) and (we set $G = 1$ henceforth)

$$M_{\text{string}} = \frac{(D-2)\Omega_{D-2}}{16\pi G} r_+ L. \quad (34)$$

The initial parameters are given by (recall $\mu = 1$),

$$m_i = 3.1, \quad v_i = 0.5, \quad b_i = 2.2, \quad a_i = 0.7. \quad (35)$$

For the final parameters, we can measure v_f and b_f by tracking the position of the outgoing blobs, and extracting the metric components in the region of the corresponding blobs. We find

$$v_f \approx 0.3, \quad b_f \approx 4.26. \quad (36)$$

We see that the outgoing BHs do not rotate, so they can be approximated Schwarzschild BHs. Their mass is then given by

$$m_f \approx 3.1. \quad (37)$$

The mass and rotation parameter of the central blob can be estimated by computing $\Omega = \beta^\phi \approx 1.5$, $g_{\phi\phi} \approx 0.25$ and comparing this with the values for a MP BH. We obtain

$$m_{\text{central}} \approx 0.07, \quad J \approx 0.009, \quad a_{\text{central}} \approx 0.32. \quad (38)$$

Collecting these results, we obtain

$$M_i \approx 7.1, J_i \approx 5.9, \quad M_f \approx 6.6, J_f \approx 4.2. \quad (39)$$

Assuming that there could be an uncertainty of 10% in the values of m_f , v_f and b_f , we obtain that about $8^{+10}_{-10}\%$ of the total mass-energy and $30^{+19}_{-25}\%$ of the angular momentum are radiated.

Numerical tests.—In view of the very high computational resources needed for the simulations presented in this work (about 2M CPU hours per run), a standard convergence analysis with two additional simulations at higher resolution is prohibitively costly. In order to achieve a practical convergence study, we apply two steps that greatly reduce the expenses. First, we consider a quantity where the continuum limit is already known, namely the Hamiltonian constraint. This reduces the number of required resolutions from three to two. Second, instead of repeating the entire simulation, we instead use the fact that the code dynamically adds resolution in the critical regions by adding extra refinement levels. More specifically, we have performed the later stages of the 6D-A simulation twice. In one case, the code adds, as instructed by the tagging criterion, an additional refinement level, the 9th level, that covers the black string region and the satellites. In the second case, we have disallowed the code from adding this level and instead let the simulation continue from its previous checkpoint with a mere 8 refinement levels. These two instances of our simulation enable us to analyse the dependence of the Hamiltonian constraint on resolution in the vicinity of the high curvature region. We note in this context that the constraint violations

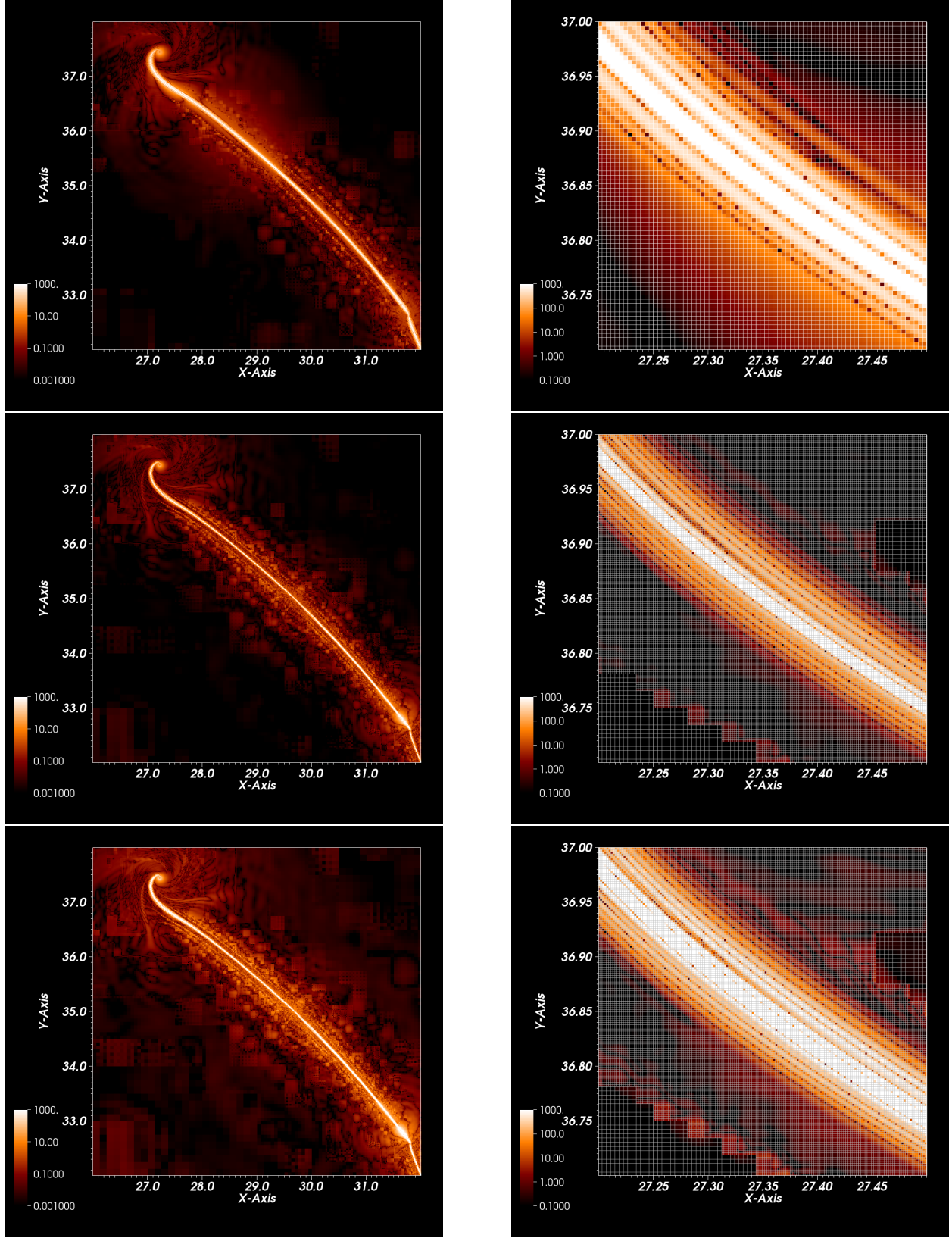


FIG. 9. *Left column:* The Hamiltonian constraint for the 6D-A simulation in the xy plane at $t = 22$. The upper panel shows the constraint obtained using 8 refinement levels only. The constraint with an additional 9th level is shown in the center panel and, amplified by a factor $Q_2 = 4$ for second-order convergence, in the bottom panel. *Right column:* A zoom-in of each of the left panels shows the constraint in a smaller region around the string. Here, we also display the grid structure in the form of a gray mesh.

rapidly decrease in the outer regions of our computational domain, as expected from the rapid fall-off of gravity in higher-dimensional spacetimes.

In Fig. 9, we show the Hamiltonian constraint for the 6D-A simulation in the xy plane at $t = 22$. In the left column of this figure, we display the upper left half of the string only for better image quality; the lower right half is obtained from reflection across the bottom right corner. Let us first compare the upper and center panels which are obtained using 8 and 9 levels, respectively. We clearly see that the string shaped region of large constraint violations is thicker for the lower resolution in the upper panel. The resulting larger constraint violations also extend into the outer regions as visible in the form of the cloud like structure surrounding the string, especially in the upper half. Both these effects are visibly reduced by the higher resolution around the string in the center panel, although at a small price: the additional refinement boundaries introduce some numerical noise visible in the form of the rectangular structures in the center panel.

In order to obtain a rough estimate of the convergence order, we show in the bottom left panel of Fig. 9 the higher resolution result amplified by a factor $Q_2 = 4$ as expected for second-order convergence, which is the dominant discretization order in the prologation operation. This amplification roughly widens the region of larger constraint violations in the bottom panel to a level comparable to the top panel. Note that we only expect this convergence in the immediate vicinity of the string, where extra refinement is present in the center and bottom panels.

In order to obtain a clearer illustration of the rate of convergence, we show in the right column of Fig. 9 the same result but now for a small region around the string, where we are now also able to display the grid structure. Again, the effect of the additional resolution near the string in the lower two panels is clearly perceptible. The comparable width of the string in the top and bottom panel furthermore indicates convergence commensurate with 2nd order around the string.

* tandrade@icc.ub.edu

† p.figueras@qmul.ac.uk

‡ U.Sperhake@damtp.cam.ac.uk

- [1] S. W. Hawking and R. Penrose, *Proc. Roy. Soc. Lond.* **A314**, 529 (1970).
- [2] R. Penrose, *Riv. Nuovo Cim.* **1**, 252 (1969), [*Gen. Rel. Grav.*34,1141(2002)].
- [3] M. W. Choptuik, *Phys. Rev. Lett.* **70**, 9 (1993).
- [4] R. Gregory and R. Laflamme, *Phys. Rev. Lett.* **70**, 2837 (1993).
- [5] J. Eggers, *Phys. Rev. Lett.* **71**, 3458 (1993).
- [6] J. Eggers, *Rev. Mod. Phys.* **69**, 865 (1997).
- [7] L. Lehner and F. Pretorius, (2011), [arXiv:1106.5184 \[gr-qc\]](https://arxiv.org/abs/1106.5184).
- [8] J. E. Santos and B. Way, *Phys. Rev. Lett.* **114**, 221101 (2015).
- [9] R. Emparan and R. C. Myers, *JHEP* **09**, 025 (2003).
- [10] O. J. C. Dias, P. Figueras, R. Monteiro, J. E. Santos, and R. Emparan, *Phys. Rev.* **D80**, 111701 (2009).
- [11] O. J. C. Dias, P. Figueras, R. Monteiro, H. S. Reall, and J. E. Santos, *JHEP* **05**, 076 (2010).
- [12] M. Shibata and H. Yoshino, *Phys. Rev.* **D81**, 021501 (2010).
- [13] M. Shibata and H. Yoshino, *Phys. Rev.* **D81**, 104035 (2010).
- [14] O. J. C. Dias, G. S. Hartnett, and J. E. Santos, *Class. Quant. Grav.* **31**, 245011 (2014).
- [15] P. Figueras, M. Kunesch, and S. Tunyasuvunakool, *Phys. Rev. Lett.* **116**, 071102 (2016), [arXiv:1512.04532 \[hep-th\]](https://arxiv.org/abs/1512.04532).
- [16] P. Figueras, M. Kunesch, L. Lehner, and S. Tunyasuvunakool, *Phys. Rev. Lett.* **118**, 151103 (2017), [arXiv:1702.01755 \[hep-th\]](https://arxiv.org/abs/1702.01755).
- [17] H. Bantilan, P. Figueras, M. Kunesch, and R. Panosso Macedo, *Phys. Rev. D* **100**, 086014 (2019), [arXiv:1906.10696 \[hep-th\]](https://arxiv.org/abs/1906.10696).
- [18] T. Andrade, R. Emparan, D. Licht, and R. Luna, *JHEP* **04**, 121 (2019), [arXiv:1812.05017 \[hep-th\]](https://arxiv.org/abs/1812.05017).
- [19] T. Andrade, R. Emparan, D. Licht, and R. Luna, *JHEP* **09**, 099 (2019), [arXiv:1908.03424 \[hep-th\]](https://arxiv.org/abs/1908.03424).
- [20] U. Sperhake, V. Cardoso, F. Pretorius, E. Berti, and J. A. González, *Phys. Rev. Lett.* **101**, 161101 (2008), [arXiv:0806.1738 \[gr-qc\]](https://arxiv.org/abs/0806.1738).
- [21] U. Sperhake, W. Cook, and D. Wang, *Phys. Rev. D* **100**, 104046 (2020), [1909.02997](https://arxiv.org/abs/1909.02997).
- [22] U. Sperhake, V. Cardoso, F. Pretorius, E. Berti, T. Hinderer, and N. Yunes, *Phys. Rev. Lett.* **103**, 131102 (2009), [arXiv:0907.1252 \[gr-qc\]](https://arxiv.org/abs/0907.1252).
- [23] D. Alic, C. Bona-Casas, C. Bona, L. Rezzolla, and C. Palenzuela, *Phys. Rev.* **D85**, 064040 (2012).
- [24] A. Weyhausen, S. Bernuzzi, and D. Hilditch, *Phys. Rev.* **D85**, 024038 (2012).
- [25] F. Pretorius, *Class. Quant. Grav.* **22**, 425 (2005).
- [26] W. G. Cook, P. Figueras, M. Kunesch, U. Sperhake, and S. Tunyasuvunakool, *Int. J. Mod. Phys.* **D25**, 1641013 (2016).
- [27] R. C. Myers and M. J. Perry, *Ann. Phys.* **172**, 304 (1986).
- [28] U. Sperhake, *Phys. Rev. D* **76**, 104015 (2007), [arXiv:gr-qc/0606079](https://arxiv.org/abs/gr-qc/0606079).
- [29] W. G. Cook, D. Wang, and U. Sperhake, *Class. Quant. Grav.* **35**, 235008 (2018), [arXiv:1808.05834 \[gr-qc\]](https://arxiv.org/abs/1808.05834).
- [30] K. Clough, P. Figueras, H. Finkel, M. Kunesch, E. A. Lim, and S. Tunyasuvunakool, *Class. Quant. Grav.* **32**, 245011 (2015).
- [31] M. Adams, P. Colella, D. Graves, J. Johnson, N. Keen, T. Ligocki, D. Martin, P. McCorquodale, D. Modiano, P. Schwartz, T. Sternberg, and B. Van Straalen, *Chombo Software Package for AMR Applications - Design Document*, Tech. Rep. LBNL-6616E (Lawrence Berkeley National Laboratory, 2015).
- [32] R. Emparan, T. Shiromizu, R. Suzuki, K. Tanabe, and T. Tanaka, *JHEP* **06**, 159 (2015), [arXiv:1504.06489 \[hep-th\]](https://arxiv.org/abs/1504.06489).
- [33] R. Emparan, R. Suzuki, and K. Tanabe, *Phys. Rev. Lett.* **115**, 091102 (2015), [arXiv:1506.06772 \[hep-th\]](https://arxiv.org/abs/1506.06772).
- [34] R. Emparan, K. Izumi, R. Luna, R. Suzuki, and K. Tanabe, *JHEP* **06**, 117 (2016), [arXiv:1602.05752 \[hep-th\]](https://arxiv.org/abs/1602.05752).
- [35] R. Emparan, (2020), [arXiv:2005.07389 \[hep-th\]](https://arxiv.org/abs/2005.07389).
- [36] H. Okawa, K.-i. Nakao, and M. Shibata, *Phys. Rev. D* **83**, 121501 (2011), [arXiv:1105.3331 \[gr-qc\]](https://arxiv.org/abs/1105.3331).
- [37] D. Pook-Kolb, O. Birnholtz, B. Krishnan, and E. Schnetter, *Phys. Rev. D* **99**, 064005 (2019), [arXiv:1811.10405 \[gr-qc\]](https://arxiv.org/abs/1811.10405).
- [38] D. Pook-Kolb, O. Birnholtz, B. Krishnan, and E. Schnetter, *Phys. Rev. D* **100**, 084044 (2019), [arXiv:1907.00683 \[gr-qc\]](https://arxiv.org/abs/1907.00683).
- [39] We would like to thank Tiago França and Chenxia Gu for kindly sharing their data with us.
- [40] There is a typo in the analogous formula for the scalar derived tensor harmonics in [], which we correct here.
- [41] Note that this basis differs from the one used in []. The reason is explained below.
- [42] V. Cardoso, O. J. Dias, and J. P. Lemos, *Phys. Rev. D* **67**, 064026 (2003), [arXiv:hep-th/0212168](https://arxiv.org/abs/hep-th/0212168).
- [43] M. Godazgar and H. S. Reall, *Phys. Rev. D* **85**, 084021 (2012), [arXiv:1201.4373 \[gr-qc\]](https://arxiv.org/abs/1201.4373).